First-principles equation of state and electronic properties of warm dense oxygen

K. P. Driver, F. Soubiran, Shuai Zhang, and B. Militzer

Citation: The Journal of Chemical Physics **143**, 164507 (2015); doi: 10.1063/1.4934348
View online: https://doi.org/10.1063/1.4934348
View Table of Contents: http://aip.scitation.org/toc/jcp/143/16
Published by the American Institute of Physics

Articles you may be interested in

Equation of state and shock compression of warm dense sodium—A first-principles study
The Journal of Chemical Physics **146**, 074505 (2017); 10.1063/1.4976559

Properties of hydrogen, helium, and silicon dioxide mixtures in giant planet interiors
Physics of Plasmas **24**, 041401 (2017); 10.1063/1.4978618

Equation of state and transport properties of warm dense aluminum by ab initio and chemical model simulations
Physics of Plasmas **24**, 013303 (2017); 10.1063/1.4973834

Path integral Monte Carlo simulations of dense carbon-hydrogen plasmas
The Journal of Chemical Physics **148**, 102318 (2018); 10.1063/1.5001208

Ab initio quantum Monte Carlo simulation of the warm dense electron gas
Physics of Plasmas **24**, 056303 (2017); 10.1063/1.4977920

First-principles equation-of-state table of beryllium based on density-functional theory calculations
Physics of Plasmas **24**, 062702 (2017); 10.1063/1.4984780

PHYSICS TODAY
WHITEPAPERS

ADVANCED LIGHT CURE ADHESIVES

Take a closer look at what these environmentally friendly adhesive systems can do

READ NOW

PRESENTED BY
MASTERBOND
ADHESIVES | SEALANTS | COATINGS

First-principles equation of state and electronic properties of warm dense oxygen

K. P. Driver,[1,a)] F. Soubiran,[1] Shuai Zhang,[1] and B. Militzer[1,2]
[1]*Department of Earth and Planetary Science, University of California, Berkeley, California 94720, USA*
[2]*Department of Astronomy, University of California, Berkeley, California 94720, USA*

(Received 30 May 2015; accepted 9 October 2015; published online 27 October 2015)

We perform all-electron path integral Monte Carlo (PIMC) and density functional theory molecular dynamics (DFT-MD) calculations to explore warm dense matter states of oxygen. Our simulations cover a wide density-temperature range of 1–100 g cm^{-3} and 10^4–10^9 K. By combining results from PIMC and DFT-MD, we are able to compute pressures and internal energies from first-principles at all temperatures and provide a coherent equation of state. We compare our first-principles calculations with analytic equations of state, which tend to agree for temperatures above 8×10^6 K. Pair-correlation functions and the electronic density of states reveal an evolving plasma structure and ionization process that is driven by temperature and density. As we increase the density at constant temperature, we find that the ionization fraction of the 1s state decreases while the other electronic states move towards the continuum. Finally, the computed shock Hugoniot curves show an increase in compression as the first and second shells are ionized. © *2015 AIP Publishing LLC.* [http://dx.doi.org/10.1063/1.4934348]

I. INTRODUCTION

Elemental oxygen is involved in a wide range of physics and chemistry throughout the universe, spanning from ambient biological processes to extreme geological and astrophysical processes. Created during stellar nucleosynthesis, oxygen is the third most abundant element in the universe and the most abundant element on Earth. In addition to its importance for life-sustaining processes, its thermodynamic, physical, and chemical properties are important to numerous fields of science. As such, oxygen has inspired a vast number of laboratory experiments and theoretical studies, which have revealed an exotic phase diagram with a number of interesting anomalies in its thermal, optical, magnetic, electrical, and acoustic properties due to its molecular and magnetic nature.[1]

At ambient conditions, oxygen exists as a diatomic molecular gas with each molecule having two unpaired electrons, resulting in a paramagnetic state. X-ray diffraction and optical experiments reveal that oxygen condenses to a molecular solid with a rich phase diagram made up of at least ten different structural phases.[1–6] Static compression experiments on the solid have been performed up to 1.3 Mbar and 650 K.[1] First-principles simulations have been used to search for structural phases up to 100 Mbar.[6] The transition to the highest-pressure phase discovered so far occurs at 96 GPa, which also drives the solid to become metallic.[7–10] A superconducting phase has also been found at 0.6 K near 100 GPa.[11] In addition, the solid phases exhibit a complex magnetic structure with various degrees of ordering due to a strong exchange interaction between O_2 molecules that becomes suppressed under pressure and acts in tandem with weak van der Waals forces holding the lattice together.[1,12,13]

Warm, dense, fluid states of oxygen have also been of great interest due to the presence of oxygen-rich compounds in inner layers of giant planets,[19–23] stellar interiors,[24,25] astrophysical processes,[26–28] and detonation products.[29] Oxygen is produced via helium burning[30] in the late stages of Sun-like star's life as well as in more massive stars. The larger weight of oxygen relative to hydrogen and helium drives its settlement towards the deepest regions of a star. An accurate equation of state (EOS) is needed to properly describe the behavior of the core of the star as well as the timing of the different nuclear processes that are highly sensitive to temperature.[30,31] Eventually, intermediate mass stars evolve into white dwarfs, which have most of their hydrogen and helium depleted, leaving a remnant composed mostly of carbon and oxygen. The core density of a white dwarf[16] is likely higher than 10^5 g/cm^3. The cooling process of the white dwarf is very similar from one white dwarf to another and the luminosity is used for cosmological chronology.[32,33] However, the accuracy of chronology measurements depends on a proper description of the thermodynamic behavior of both carbon and oxygen.[34] Moreover, as the third most abundant element in the solar system,[35] oxygen has a significant presence in planet interiors and can exist in a partially ionized state in giant planets. Therefore, the electronic and thermodynamic behavior of oxygen at high pressures and temperatures is important for obtaining the correct fluid and magnetic behavior in planetary, stellar, and stellar remnant models.[36]

Shock-compressed fluid states of oxygen have been measured under dynamic compression up to 1.9 Mbar (four-fold compression) and 7000 K, which revealed a metallic transition in the molecular fluid at 1.2 Mbar and 4500 K.[37] Density functional theory molecular dynamics (DFT-MD)

a)Electronic mail: kdriver@berkeley.edu; URL: http://militzer.berkeley.edu/~driver/.

 © 2015 AIP Publishing LLC

simulations suggest that disorder in the fluid lowers the metallization pressure to as low as 30 GPa with molecular dissociation above 80 GPa.[38] Measurements of Hugoniots have reached 140 GPa[39–41] and indicate that oxygen molecules become dissociated in a pressure range of 80-120 GPa at temperatures over several thousand Kelvin. Using classical pair-potential simulations,[42–44] some general agreement is found with the measured Hugoniots; however, a fully quantum-mechanical treatment is needed to accurately simulate the electronic and structural behavior of the fluid.

Historically, a lack of development in first-principles methodology for the warm dense matter regime has largely prevented highly accurate theoretical exploration of fluid oxygen at extreme conditions, and, hence, further improvements in EOS and Hugoniot curves. DFT-MD has been used to explore the structural and electronic behavior of the fluid state[38,45] up to temperatures of 16×10^3 K and densities up to 4.5 g cm^{-3}. Massacrier *et al.*[46] investigated the properties of oxygen for a density-temperature range of 10^{-3}–10^4 g cm^{-3} and 10^5–10^6 K, using an average ion model. They showed, for instance, that the complete pressure-ionization of fluid oxygen cannot be expected until the system reaches a density of 1000 g cm^{-3}.

In order to address the challenges of first-principles simulations for warm dense matter, we have been developing the path integral Monte Carlo (PIMC) methodology in recent years for the study of heavy elements in warm, dense states.[47–50] Here, we apply our PIMC methodology along with DFT-MD to extend the first principles exploration of warm dense fluid oxygen to a much wider density-temperature range (1–100 g cm^{-3} and 10^4–10^9 K) than has been previously explored by DFT-MD alone.

In Section II, we cover details of the PIMC and DFT-MD methodology specific to our oxygen simulations. In Section III, we discuss the EOS constructed from PIMC and DFT-MD and show that both methods agree for at least one of the temperatures in the range of 2.5×10^5–1×10^6 K. In Section IV, we characterize the structure of the plasma and the ionization process by examining pair-correlation functions of electrons and nuclei as a function of temperature and density. In Section V, we discuss the electronic density of states (DOS) as a function of density and temperature to provide further insight into the ionization process. In Section VI, we discuss predictions for the shock Hugoniot curves. Finally, in Section VII, we summarize and conclude our results.

II. SIMULATION METHODS

PIMC[47,51] is currently the state-of-the-art first-principles method for simulating materials at temperatures in which properties are dominated by excited states. It is the only method able to accurately treat all the effects of bonding, ionization, exchange-correlation, and quantum degeneracy that simultaneously occur in the warm dense matter regime.[52] PIMC is based on thermal density matrix formalism, which is efficiently computed with Feynman's imaginary time path integrals. The density matrix is the natural operator to use for computing high-temperature observables because it explicitly includes temperature in a many-body formalism.

The PIMC method stochastically solves the full, finite-temperature quantum many-body problem by treating electrons and nuclei equally as quantum paths that evolve in imaginary time without invoking the Born-Oppenheimer approximation. For our PIMC simulations, the Coulomb interaction is incorporated via pair density matrices derived from the eigenstates of the two-body Coulomb problem[51,53] appropriate for oxygen. Furthermore, in contrast to DFT-MD as described below, the efficiency of PIMC increases with temperature as particles behave more classical-like and fewer time slices are needed to describe quantum mechanical many-body correlations, scaling inversely with temperature.

PIMC uses a minimal number of controlled approximations, which become vanishingly small with increased temperature and by using appropriate convergence of the time-step and system size. The only uncontrolled approximation is the employment of a fixed nodal surface to avoid the fermion sign problem.[54] Current state-of-the art PIMC calculations employ a free-particle nodal structure, which would perfectly describe a fully ionized system. However, we have shown that PIMC employing free-particle nodes even produces reliable results at surprising low temperatures in partially ionized hydrogen,[55] carbon,[48] water,[48] and neon.[50] As a general rule, we find free-particle nodes are sufficient for systems comprised of partially-ionized 2s states.[48]

A sufficiently small PIMC time step is determined by converging total energy as a function of time step until the energy changes by less than 0.5%, which is shown in Table SI of the supplementary material.[56] We use a time step of 1/256 Ha^{-1} for temperatures below 4×10^6 K and, for higher temperatures, we decrease the time step as $1/T$, as the efficiency of PIMC increases linearly with T as path lengths decrease. The number of time slices we use in the path integral range from 323 at lowest temperature to 5 at the highest temperature. In order to minimize finite size errors, the internal energy and pressure is converged to better than 0.4% when comparing 8- and 24-atom simple cubic simulation cells, which is shown in Table SII of the supplementary material.[56] We therefore perform all PIMC calculations in 8-atom cells, as PIMC scales as N^2, where N is the number of particles. A typical calculation uses a bisection level[51] of 5 and achieves a statistical error in the energy and pressure that is less than 0.1%.

For lower temperatures ($T < 1 \times 10^6$ K), DFT-MD[57] is the most efficient state-of-the-art first-principles method. DFT formalism provides an exact mapping of the many body problem onto a single particle problem, but, in practice, employs an approximate exchange-correlation potential to describe many body electron physics. In the WDM regime, where temperatures are at or above the Fermi temperature, the exchange-correlation functional is not explicitly designed to accurately describe the electronic physics.[58] However, in previous PIMC and DFT-MD work on helium,[47] carbon,[48] and water,[48] and neon,[50] DFT functionals are shown to be accurate even at high temperatures.

DFT incorporates effects of finite electronic temperature into calculations by using a Fermi-Dirac function to allow for thermal occupation of single-particle electronic states.[59] As temperature grows large, an increasing number of bands are required to account for the increasing occupation of excited

states in the continuum, which typically causes the efficiency of the algorithm to become intractable at temperatures beyond 1×10^6 K. Orbital-free density functional methods aim to overcome such thermal band efficiency limitations, but several challenges remain to be solved.[60] In addition, pseudopotentials, which replace the core electrons in each atom and improve efficiency, may break down at temperatures where core electrons undergo excitations.

Depending on the density, we employ two different sets of DFT-MD simulations for our study of oxygen. At densities below 15 g cm^{-3}, the simulations were performed with the Vienna *Ab initio* Simulation Package (VASP)[61] using the projector augmented-wave (PAW) method.[62] The VASP DFT-MD uses an NVT ensemble regulated with a Nosé-Hoover thermostat. Exchange-correlation effects are described using the Perdew-Burke-Ernzerhof[63] generalized gradient approximation. Electronic wave functions are expanded in a plane-wave basis with a energy cutoff of at least 1000 eV in order to converge total energy. Size convergence tests up to a 24-atom simulation cell at temperatures of 10 000 K and above indicate that total energies are converged to better than 0.1% in a 24-atom simple cubic cell. We find, at temperatures above 250 000 K, 8-atom supercell results are sufficient since the kinetic energy far outweighs the interaction energy at such high temperatures. The number of bands in each calculation is selected such that thermal occupation is converged to better than 10^{-4}, which requires up to 8000 bands in a 24-atom cell at 1×10^6 K. All simulations are performed at the Γ-point of the Brillouin zone, which is sufficient for high temperature fluids, converging total energy to better than 0.01% relative to a comparison with a grid of k-points.

For densities above 15 g cm^{-3}, we had to construct a new pseudopotential in order to prevent the overlap of the PAW-spheres. We therefore used the ABINIT package[64] for which it is possible to build a specific PAW-pseudopotential using the AtomPAW plugin.[65] We built a hard all-electron PAW pseudopotential with a cutoff radius of 0.4 Bohr. We checked the accuracy of the pseudopotential by reproducing the results with an all-electron, full-potential, linearised, augmented-planewave (FP-LAPW) code, Elk.[66] With this pseudopotential, we performed DFT-MD with ABINIT for a 24-atom cell up to 100 g cm^{-3} and 1×10^6 K. The hardness of the pseudopotential required an plane-wave energy cutoff of at least 6800 eV.

III. EQUATION OF STATE RESULTS

In this section, we report our EOS results for six densities of 2.486 34, 3.630 46, 7.261 76, 14.8632, 50.00, and 100.00 g cm^{-3} and for a temperature range of 10^4–10^9 K. The six isochores are shown in Figure 1 and are discussed in more detail in Section VI. These conditions are relevant for the modeling of stars and white dwarfs as can be seen in Figure 1.

Figure 2 compares pressures obtained for oxygen from PIMC, DFT-MD, and from analytic Chabrier-Potekhin[67] and Debye-Hückel[68] models. Pressures, P, are plotted relative to a fully ionized Fermi gas of electrons and ions with pressure, P_0, in order to compare only the excess pressure contributions that result from particle interactions. In general, PIMC and DFT-MD pressures differ by at most 2%, and often much less for

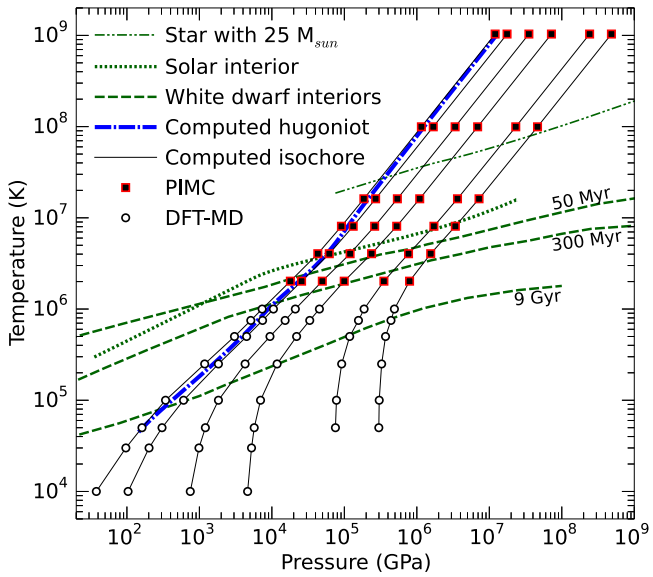

FIG. 1. Temperature-pressure conditions for the PIMC and DFT-MD calculations along six isochores corresponding to the densities of 2.486 34, 3.630 46, 7.261 76, 14.8632, 50.00, and 100.00 g cm^{-3}. The dashed-dotted line shows the Hugoniot curve for an initial density of $\rho_0 = 0.6671$ g cm^{-3}. For comparison, we also plotted the interior profile of the current-day Sun[14] as well as the profile of a 25 M$_\odot$ star at the end of its helium burning time.[15] The green dashed lines show the interior profile of a 0.6 M$_\odot$ carbon-rich white dwarf at three different stages of its cooling process.[16–18]

at least one temperature in the range of 2.5×10^5–1×10^6 K. PIMC converges to the weakly interacting plasma limit along with the Chabrier-Potekhin and Debye-Hückel models.

Figure 3 compares internal energies, E, plotted relative to the internal energy of a fully ionized Fermi gas, E_0. PIMC and DFT-MD results for excess internal energy differ by at most 2%, and much less in most cases for at least one temperature in the range of 2.5×10^5–1×10^6 K. PIMC extends the energies to the weakly interacting plasma limit at high temperatures, in agreement with the Potekhin and Debye-Hückel models.[68]

Together, Figs. 2 and 3 show that the DFT-MD and PIMC methods form a coherent equation of state over all temperatures ranging from the regime of warm dense matter to the weakly interacting plasma limit. The agreement between PIMC and DFT-MD indicates that DFT exchange-correlation potential remains valid even at high temperatures and that the PIMC free-particle nodal approximation is valid for a sufficient ionization fraction of the 2s state. The analytic Chabrier-Potekhin and Debye-Hückel models agree with PIMC to temperatures as low as 8×10^6 K. The Debye-Hückel model appears to have better agreement with PIMC at low densities, while the Chabrier-Potekhin model agrees better with PIMC at high densities. Neither analytic models includes bound states and, therefore, cannot describe low temperature conditions.

Table I provides the densities, temperatures, pressures, and energies used to construct our equation of state. The VASP DFT-MD energies have been shifted by 74.9392 Ha/atom in order to bring the PAW-PBE pseudopotential energy in alignment with all-electron energies that we report with PIMC computations. The shift was calculated by performing an all electron atomic calculation with a pseudopotential generation code, Opium[69] and a corresponding isolated-atom calculation in VASP.

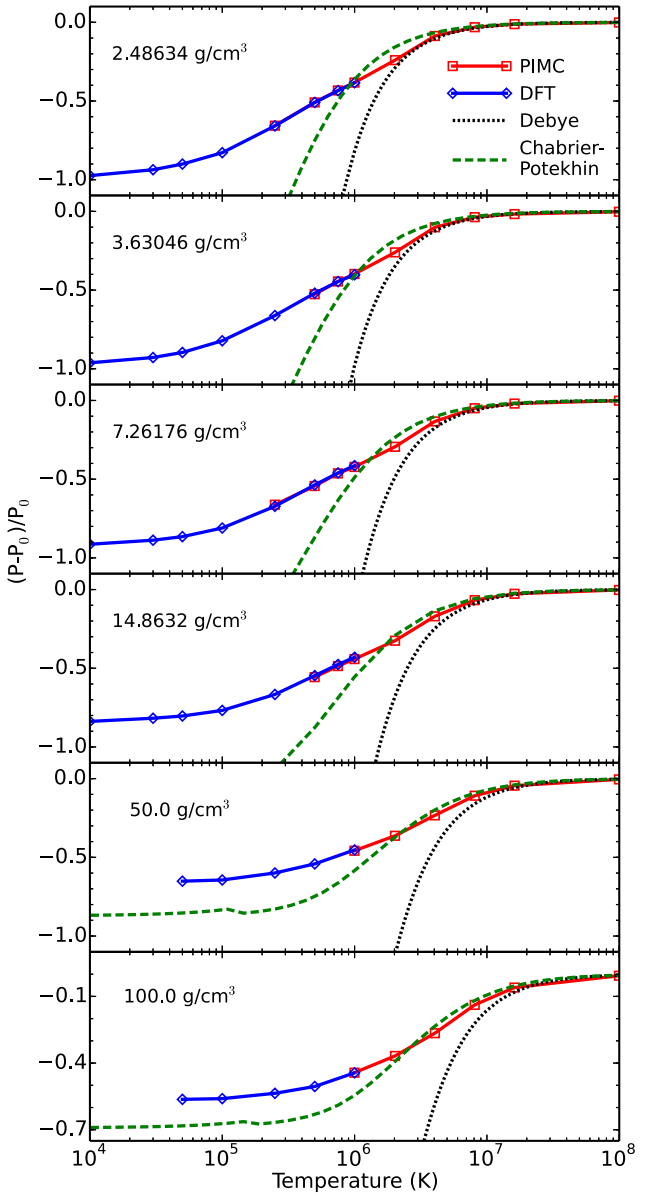

FIG. 2. Comparison of excess pressure relative to the ideal Fermi gas plotted as a function of temperature for oxygen.

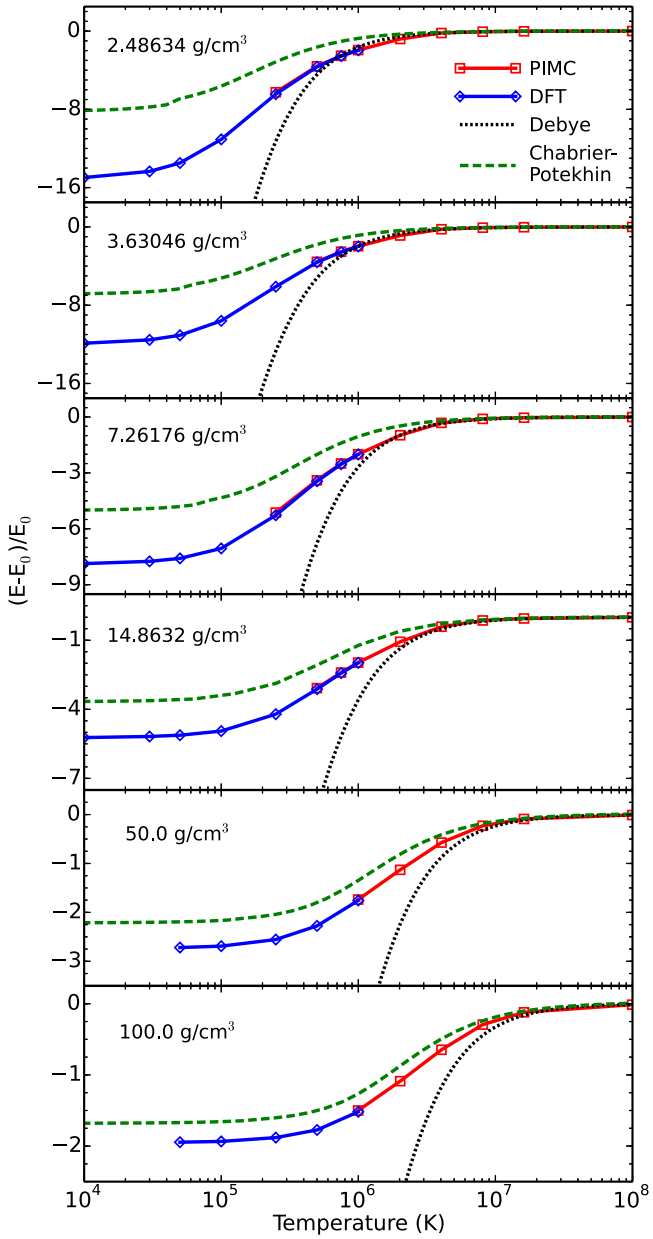

FIG. 3. Comparison of excess internal energies relative to the ideal Fermi gas plotted as a function of temperature for oxygen.

Comparison of the PIMC and DFT-MD pressures and internal energies in Table I indicates that there is roughly a 2% discrepancy in their predicted values at temperatures of 1×10^6 K. Potential sources of this discrepancy include: (1) the use of free particle nodes in PIMC, (2) the exchange-correlation functional in DFT, and (3) the use of a pseudopotential in DFT. While it is difficult to determine the size of the nodal and exchange-correlation errors, comparison of our VASP calculations with all-electron, PAW ABINIT calculations at 1×10^6 K indicates that roughly one third of the discrepancy is due to the use of frozen 1s core in the VASP DFT-MD pseudopotential, which leaves out effects of core excitations.

IV. PAIR-CORRELATION FUNCTIONS

In this section, we study pair-correlation functions[70] in order to understand the evolution of the fluid structure and ionization in oxygen plasmas as a function of temperature and density.

Figure 4 shows the nuclear pair-correlation functions, $g(r)$, computed with PIMC over a temperature range of 2×10^6–1.034×10^{12} K and a density range of 2.486–100.0 g cm^{-3}. Atoms are kept farthest apart at low temperatures due to a combination of Pauli exclusion among bound electrons and Coulomb repulsion. As temperature increases, kinetic energy of the nuclei increases, making it more likely to find atoms at close range, and, in addition, the atoms become increasingly ionized, which gradually minimizes the effects of Pauli repulsion. As density increases, the likelihood of finding two nuclei at close range is significantly increased. For the highest density and lowest temperature, the peak in the pair-correlation function reaches a value of 1.2, indicating a moderately structured fluid.

TABLE I. EOS table of oxygen pressures and internal energies at density-temperature conditions simulated in this work. The numbers in parentheses indicate the statistical uncertainties of the DFT-MD and PIMC simulations.

ρ (g cm^{-3})	T (K)	P (GPa)	E (Ha/atom)
2.486 34[a]	1 034 730 000	12 031 695(879)	44 227(3)
2.486 34[a]	99 497 670	1 155 684(608)	4242(2)
2.486 34[a]	16 167 700	185 881(73)	674.57(29)
2.486 34[a]	8 083 850	91 166(21)	323.90(9)
2.486 34[a]	4 041 920	43 037(12)	138.71(6)
2.486 34[a]	2 020 960	17 999(15)	16.06(7)
2.486 34[a]	998 004	7336(9)	−41.43(4)
2.486 34[b]	1 000 000	7339(6)	−42.41(2)
2.486 34[a]	748 503	5118(11)	−50.66(4)
2.486 34[b]	750 000	5119(5)	−51.84(18)
2.486 34[a]	500 000	3044(11)	−59.30(4)
2.486 34[b]	500 000	3049(5)	−60.58(3)
2.486 34[a]	250 000	1189(12)	−66.94(5)
2.486 34[b]	250 000	1183(3)	−69.293(3)
2.486 34[b]	100 000	341(1)	−73.635(1)
2.486 34[b]	50 000	161(1)	−74.571(1)
2.486 34[b]	30 000	97(1)	−74.811(1)
2.486 34[b]	10 000	38(1)	−75.015(1)
3.630 46[a]	1 034 730 000	17 566 926(1904)	44 223(5)
3.630 46[a]	99 497 670	1 685 108(750)	4235(2)
3.630 46[a]	16 167 700	269 993(107)	669.34(28)
3.630 46[a]	8 083 850	132 427(35)	320.24(11)
3.630 46[a]	4 041 920	61 955(18)	132.56(6)
3.630 46[a]	2 020 960	25 689(28)	10.67(8)
3.630 46[a]	998 004	10 569(14)	−42.93(4)
3.630 46[b]	1 000 000	10 507(14)	−44.13(2)
3.630 46[a]	748 503	7433(14)	−51.81(4)
3.630 46[b]	750 000	7443(8)	−52.79(5)
3.630 46[a]	500 000	4414(15)	−60.15(4)
3.630 46[b]	500 000	4483(5)	−61.412(6)
3.630 46[b]	250 000	1831(3)	−69.658(2)
3.630 46[b]	100 000	605(2)	−73.686(2)
3.630 46[b]	50 000	305(1)1	−74.565(1)
3.630 46[b]	30 000	202(2)	−74.797(1)
3.630 46[b]	10 000	104(1)	−74.992(1)
7.261 76[a]	1 034 730 000	35 142 831(2985)	44 227(4)
7.261 76[a]	99 497 670	3 374 099(1777)	4237(2)
7.261 76[a]	16 167 700	538 734(172)	664.43(26)
7.261 76[a]	8 083 850	261 808(75)	311.36(11)
7.261 76[a]	4 041 920	120 041(34)	119.03(5)
7.261 76[a]	2 020 960	49 637(51)	1.74(7)
7.261 76[a]	998 004	20 964(31)	−45.53(4)
7.261 76[b]	1 000 000	21 301(20)	−46.16(4)
7.261 76[a]	748 503	15 122(42)	−53.17(5)
7.261 76[b]	750 000	15 236(21)	−54.51(2)
7.261 76[a]	500 000	9262(24)	−61.27(3)
7.261 76[b]	500 000	9424(10)	−62.652(7)
7.261 76[a]	250 000	4405(44)	−67.78(5)
7.261 76[b]	250 000	4268(5)	−70.098(2)
7.261 76[b]	100 000	1831(3)	−73.613(2)
7.261 76[b]	50 000	1210(2)	−74.382(2)
7.261 76[b]	30 000	986(5)	−74.606(2)
7.261 76[b]	10 000	749(1)	−74.813(1)
14.863 2[a]	1 034 730 000	71 917 073(5787)	44 217(4)
14.863 2[a]	99 497 670	6 899 765(3226)	4230(2)
14.863 2[a]	16 167 700	1 096 035(364)	655.35(24)
14.863 2[a]	8 083 850	527 445(141)	299.20(10)
14.863 2[a]	4 041 920	237 350(67)	103.41(5)
14.863 2[a]	2 020 960	99 599(98)	−5.97(6)
14.863 2[a]	998 004	44 297(52)	−47.32(3)
14.863 2[b]	1 000 000	45 274(64)	−47.95(4)
14.863 2[a]	748 503	32 595(59)	−54.80(3)
14.863 2[b]	750 000	33 293(69)	−55.76(4)
14.863 2[a]	500 000	21 447(56)	−61.86(3)
14.863 2[b]	500 000	21 945(35)	−63.21(1)
14.863 2[b]	250 000	11 803(11)	−69.884(4)
14.863 2[b]	100 000	6975(7)	−72.907(3)
14.863 2[b]	50 000	5705(6)	−73.590(2)
14.863 2[b]	30 000	5239(4)	−73.815(1)
14.863 2[b]	10 000	4626(8)	−74.057(1)
50.000 0[a]	1 034 730 000	241 912 168(8061)	44 208(1)
50.000 0[a]	99 497 670	23 165 568(7204)	4215(1)
50.000 0[a]	16 167 700	3 638 714(751)	633.85(14)
50.000 0[a]	8 083 850	1 721 016(318)	272.08(6)
50.000 0[a]	4 041 920	768 044(164)	78.29(3)
50.000 0[a]	2 020 960	351 315(214)	−13.11(4)
50.000 0[a]	998 004	185 345(210)	−46.12(4)
50.000 0[c]	1 000 000	187 281(611)	−47.36(11)
50.000 0[c]	500 000	118 441(752)	−60.27(11)
50.000 0[c]	250 000	91 835(1078)	−65.16(15)
50.000 0[c]	100 000	77 796(541)	−67.49(7)
50.000 0[c]	50 000	75 320(609)	−67.90(8)
100.000[a]	1 034 730 000	483 702 750(18 188)	44 193(2)
100.000[a]	99 497 670	46 258 880(13 163)	4201(1)
100.000[a]	16 167 700	7 213 882(1458)	617.35(13)
100.000[a]	8 083 850	3 396 956(706)	254.73(7)
100.000[a]	4 041 920	1 553 594(378)	68.31(4)
100.000[a]	2 020 960	793 543(497)	−10.07(5)
100.000[a]	998 004	490 625(1050)	−40.28(10)
100.000[c]	1 000 000	490 505(1367)	−41.78(12)
100.000[c]	500 000	369 913(2987)	−52.88(24)
100.000[c]	250 000	326 893(1556)	−56.75(12)
100.000[c]	100 000	302 710(1091)	−58.79(8)
100.000[c]	50 000	298 808(1064)	−59.13(8)

[a]PIMC.
[b]VASP-MD.
[c]ABINIT-MD with a small-core, PAW pseudopotentials.

Figure 5 compares the nuclear pair-correlation functions of PIMC and DFT at a temperature of 1×10^6 K in an 8-atom cell at a density of 14.8632 g cm^{-3}. The overlapping $g(r)$ curves verify that PIMC and DFT predict consistent structural properties.

Figure 6 shows nucleus-electron pair correlation functions. Electrons are most highly correlated with the nuclei at low temperature and high density, reflecting a lower ionization fraction. As temperature increases, electrons are thermally excited and gradually become unbound, decreasing their correlation with the nuclei. As the density is increased, the electrons are more likely to reside near the nuclei, indicating that the ionization of the 1s state is suppressed with increasing density.

Figure 7 shows the integral of the nucleus-electron pair correlation function, $N(r)$, which represents the average number of electrons within a sphere of radius r around a given nucleus,

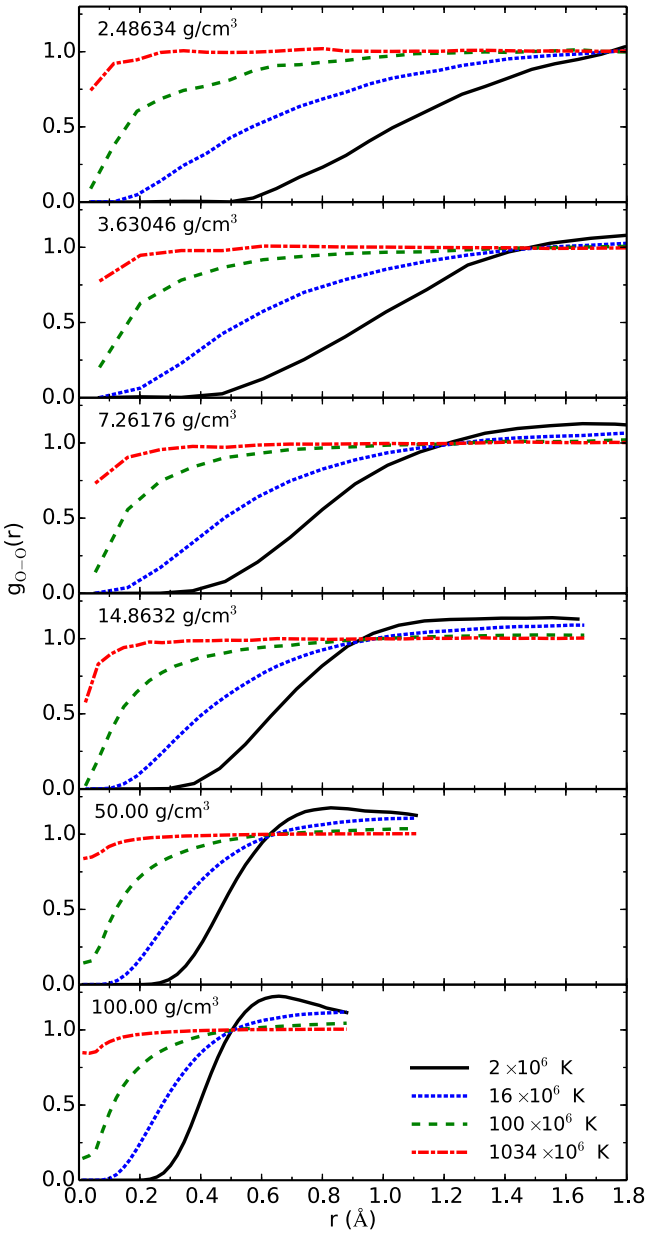

FIG. 4. Nuclear pair-correlation functions for oxygen from PIMC over a wide range of temperatures and densities.

$$N(r) = \left\langle \frac{1}{N_I} \sum_{e,I} \theta(r - |\vec{r}_e - \vec{r}_I|) \right\rangle, \tag{1}$$

where the sum includes all electron-ion pairs and θ represents the Heaviside function. At the lowest temperature, 1×10^6 K, we find that the 1s core state is always fully occupied, as it agrees closely with the result of an isolated 1s state. As temperature increases, the atoms are gradually ionized and electrons become unbound, causing $N(r)$ to decrease. As density increases, an increasingly higher temperature is required to fully ionize the atoms, confirming that the 1s ionization fraction decreases with density as seen in Fig. 6. The 1s state is thus not affected by pressure ionization in the density range of consideration. As we will explain the density of states section, the ionization of the 1s state is suppressed because with increasing density, the Fermi energy increases more rapidly than energy of the 1s state.

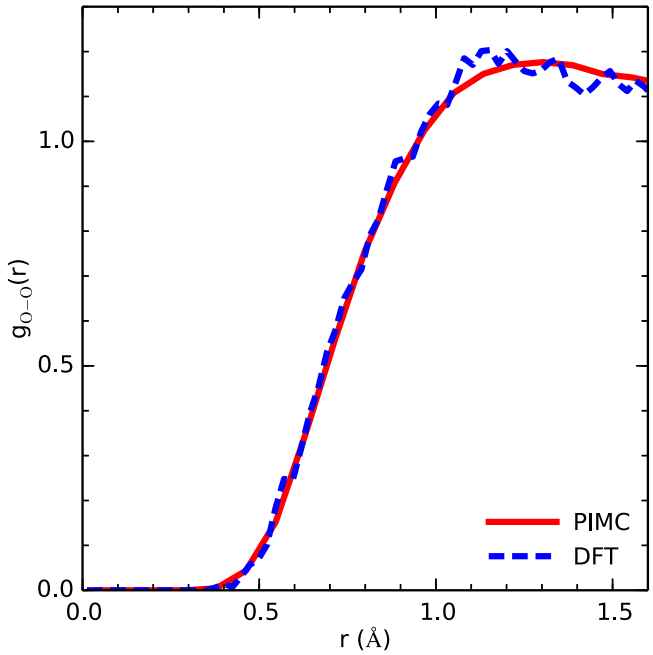

FIG. 5. Comparison of PIMC and DFT nuclear pair-correlation functions for oxygen at a temperature of 1×10^6 K and a density of 14.8632 g cm^{-3}.

Figure 8 shows electron-electron pair correlations for electrons having opposite spins. The function is multiplied by the particle density, ρ, in units of g cm^3, so that the integral under the curves is proportional to the number of electrons. The electrons are most highly correlated for low temperatures, which reflects that multiple electrons occupy bound states at one nucleus. As temperature increases, electrons are thermally excited, decreasing the correlation among each other. Correlation at short distances increases with density, consistent with a lower ionization fraction.

Figure 9 shows electron-electron pair correlations for electrons with parallel spins. The positive correlation at ~2.5 Å for $T \leq 2 \times 10^6$ K reflects that different electrons with parallel spins are bound to a single nucleus. For short separations, Pauli exclusion takes over and the functions decay to zero. The ordering of the g(r) curves changes with respect to temperature as density increases due to a competition between Coulomb and kinetic effects, coupled with the effects of ionization. When the density is 50 and 100 g cm^{-3}, pressure ionization causes the correlation to approach that of an ideal fluid, and increasing temperature further only strengthens kinetic effects. We interpret this change as pressure ionization of the second and third electron shells. As temperature increases, electrons become less bound, which also causes the correlation to become more like an ideal fluid.

V. ELECTRONIC DENSITY OF STATES

In this section, we report DFT-MD results for the electronic DOS of fluid oxygen as a function of temperature and density in order to gain further insight into the temperature- and pressure-ionization.

In order to closely examine the physics of pressure-ionization of the 1s and higher states, we computed DOS

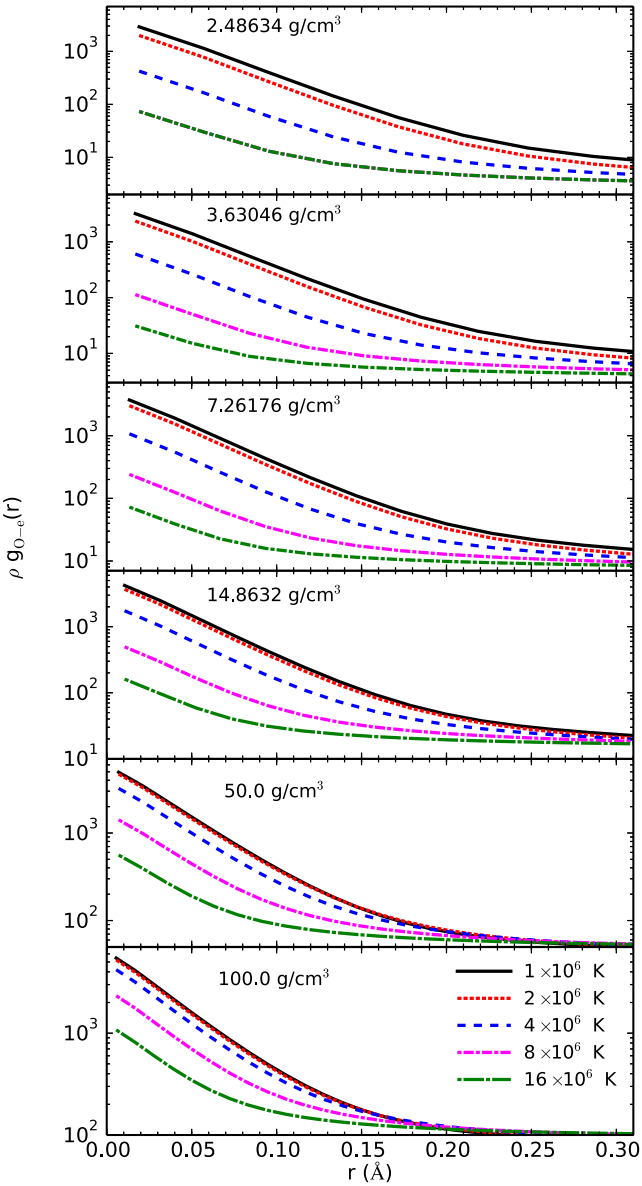

FIG. 6. The nucleus-electron pair-correlation functions for oxygen computed with PIMC.

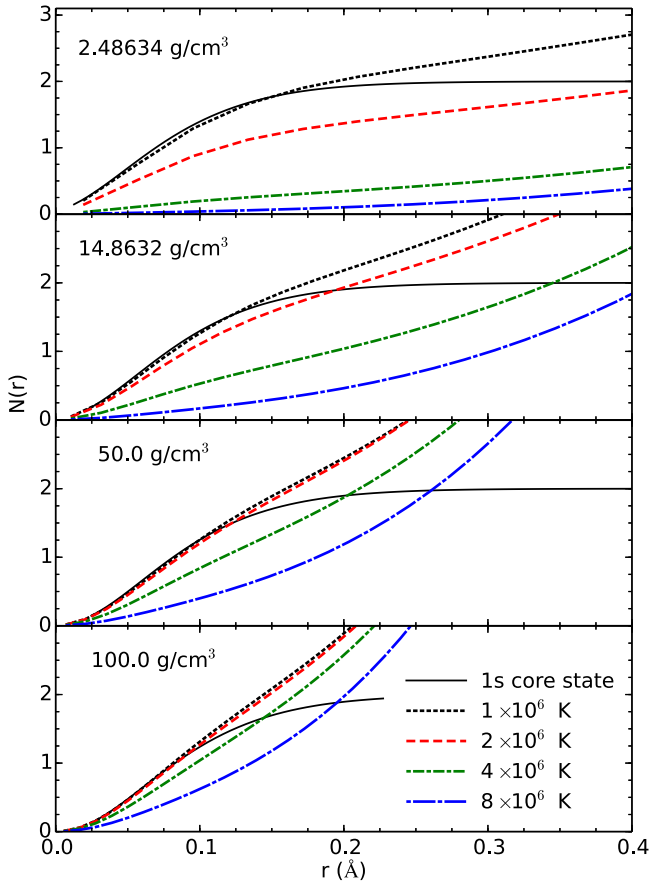

FIG. 7. Number of electrons contained in a sphere of radius, r, around an oxygen nucleus. PIMC data at four temperatures is compared with the analytic 1s core state.

curves using the all-electron, PAW potential we created for use with the ABINIT code. Figure 10 shows examples of the DOS for oxygen at densities between 2.49 and 100 g cm^{-3} at a fixed temperature of 100 000 K. For comparison, we show the result for an isolated oxygen atom. Since we used the all-electron pseudo-potential, we can see the bands related to the 1s or K shell. For the isolated atom, we also clearly see the 2s or L_I as well as the L_{II} and L_{III} states. The locations of the K and L_I shells for the isolated atom are consistent with the binding energies of 19.97 and 1.53 Ha, respectively, that can be found in the literature.[71]

As density increases, the L sub-shells are shifted towards higher energy, merging together as they shift into the continuum. This effect is referred to as the pressure ionization of oxygen, also described by Massacrier *et al.*[46] As the density increases, the K shell is also shifted to higher energies and broadens significantly. Nevertheless, the K shell remains a well defined state even at 100 g cm^{-3}. The Fermi energy is also shifted towards higher energy values as the density increases. We observe that the Fermi energy shifts more than the K-shell energy, and, hence, the energy difference between the 1s states and unoccupied states increases with the density. Therefore, it is more difficult to temperature-ionize the K shell at higher density and no pressure-ionization occurs for the 1s state. This is consistent with the observations we made for the electron-nuclei pair distribution function in Fig. 6.

Figure 11 shows the temperature dependence of the DOS at a fixed density of 7.261 76 g cm^{-3}. Results were obtained from VASP by averaging over at least 10 uncorrelated snapshots chosen from a DFT-MD trajectory. Smooth curves were obtained by using a $4 \times 4 \times 4$ k-point grid and applying a Gaussian smearing of 2 eV. The eigenvalues of each snapshot were shifted so that the Fermi energies align at zero, and the integral of the DOS is normalized to 1. The DOS curves show a large peak representing the atomic-like 2s and 2p states, followed by a dip in states, which is then followed by a continuous spectrum of conducting states. The Fermi energy plays the role of the chemical potential in the Fermi-Dirac distribution, which shifts towards more negative values as the temperature is increased. Because we subtract the Fermi energy from the eigenvalues, the peak shifts to higher energies with increasing temperature. The fact that the peaks are embedded into a dense, continuous spectrum of eigenvalues indicates that they are conducting states.

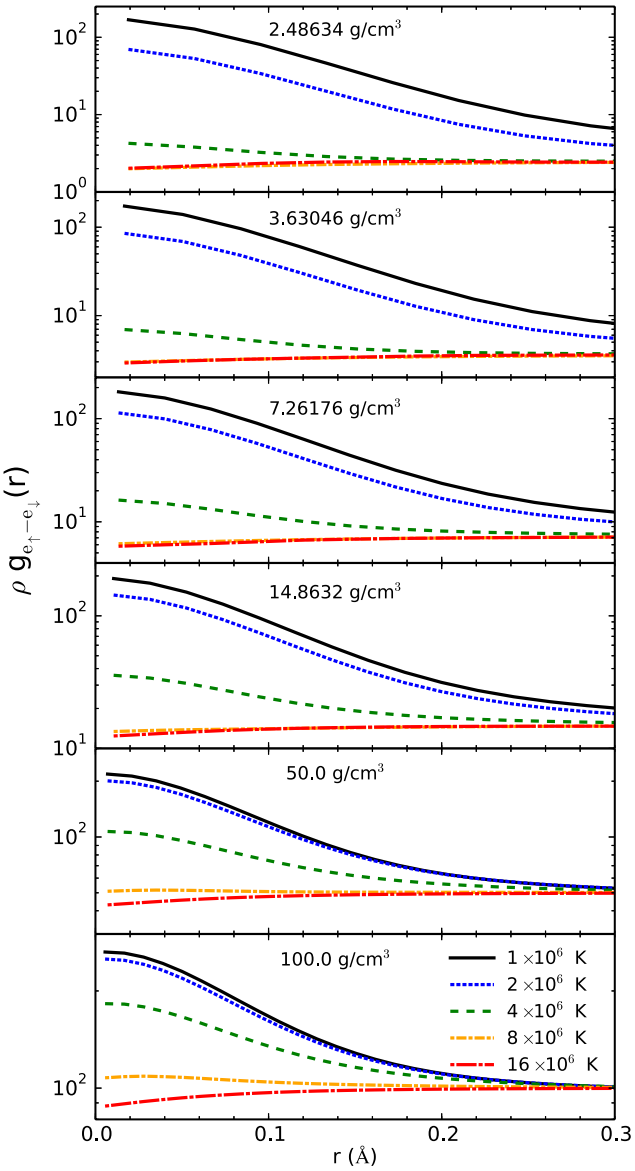

FIG. 8. The electron-electron pair-correlation functions (multiplied by ρ) for electrons with opposite spins computed with PIMC.

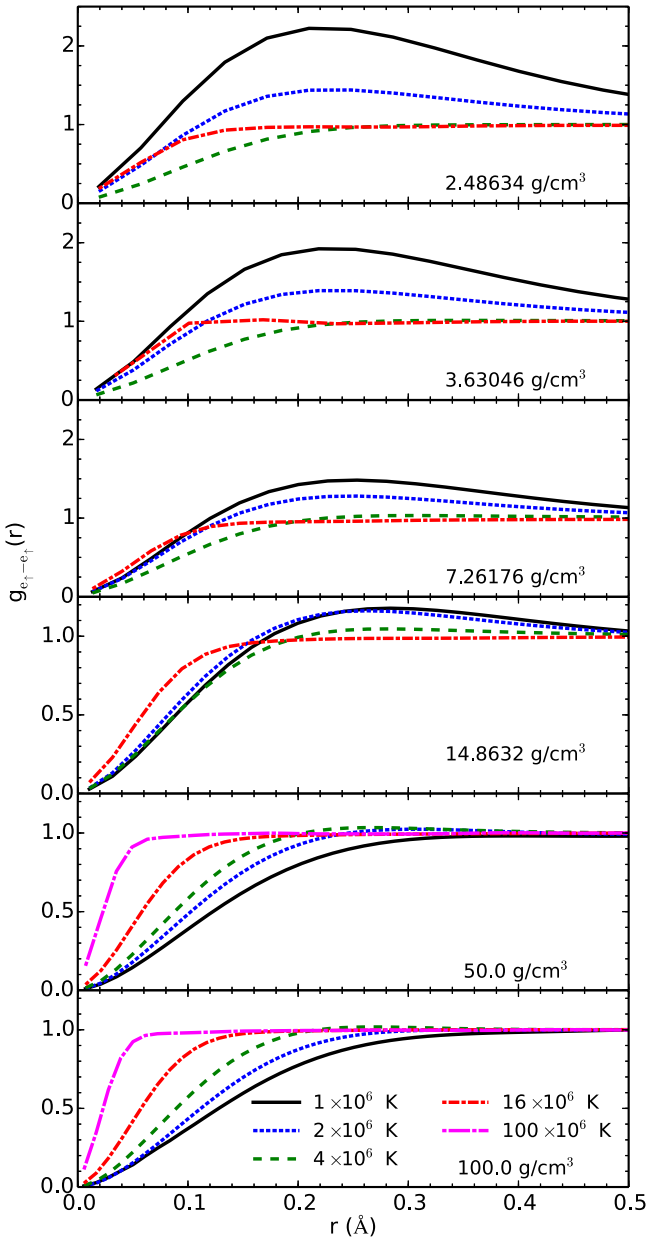

FIG. 9. The electron-electron pair-correlation functions for electrons with parallel spins computed with PIMC.

VI. SHOCK COMPRESSION

Dynamic shock compression experiments are widely used for measuring equation of state and other physical properties of hot, dense fluids. Commonly, shock experiments determine the Hugoniot, which is the locus of final states that can be obtained from different shock velocities. A few Hugoniot measurements have been made for oxygen in an effort to understand its metallic transition and determine its role in astrophysical processes.[39–41] Density functional theory has been validated by experiments as an accurate tool for predicting the shock compression of different materials.[45,72]

In the course of a shock wave experiment, a material whose initial state is characterized by an internal energy, pressure, and volume, (E_0, P_0, V_0) evolves to a final state denoted by (E, P, V) while conserving mass, momentum, and energy. This leads to the Rankine-Hugoniot relation,[73]

$$H = (E - E_0) + \frac{1}{2}(P + P_0)(V - V_0) = 0. \qquad (2)$$

Here, we compute the Hugoniot for oxygen from the first-principles EOS data we showed in Table I. The pressure and internal energy data points were interpolated with bi-cubic spline functions in $\rho - T$ space. For the initial state of the principal Hugoniot curve, we computed the energy of an oxygen molecule at $P_0 = 0$, $E_0 = -150.247\,327$ Ha/O_2, and chose $V_0 = 318.612$ Å^3. We chose a density of 0.6671 g cm^{-3} for solid oxygen in the cubic, γ phase. The resulting Hugoniot curve has been plotted in T-P and P-ρ spaces in Figs. 1 and 12, respectively.

Samples in shock wave experiments may be pre-compressed inside of a diamond anvil cell in order to reach much higher final densities than possible with a sample at ambient conditions. This technique allows shock wave experiments to probe density-temperature consistent with planetary and stellar interiors.[74] Therefore, we repeat our

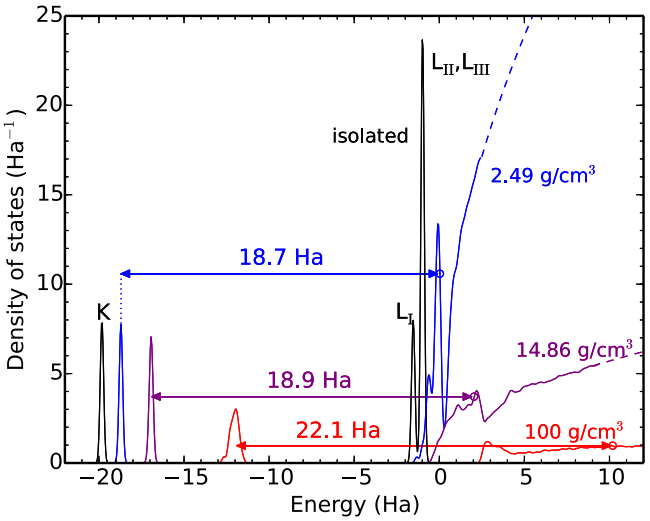

FIG. 10. Electronic density of states of dense, fluid oxygen using an all-electron, PAW pseudo-potential. The solid lines represent all available states for the isolated atom as well as three other densities at a temperature of 1×10^5 K. The curves are normalized such that the occupied DOS integrates to 8. The K, L_I, L_{II} and L_{III} identify the electronic shells and sub-shells for the isolated atoms. The open circle on each curve stands for the DOS at the Fermi energy level. The arrows show the energy difference between the K-shell and the Fermi energy for the different densities.

Hugoniot calculation starting with initial densities ranging from a 1 to a 25-fold increase of the ambient density. Figure 12 shows the resulting family of Hugoniot curves. While starting from the ambient density leads to a maximum shock density of 3.5 g cm^{-3}, a 25-fold pre-compression yields a much higher maximum shock density of 71 g cm^{-3}, as expected. However, such extreme densities can be reached more easily with triple shock experiments as our example in Fig. 12 illustrates. We used the first compression maximum on the principal Hugoniot curve ($\rho = 3.182$ g cm^{-3}, $P = 2535$ GPa, $T = 358\,600$ K)

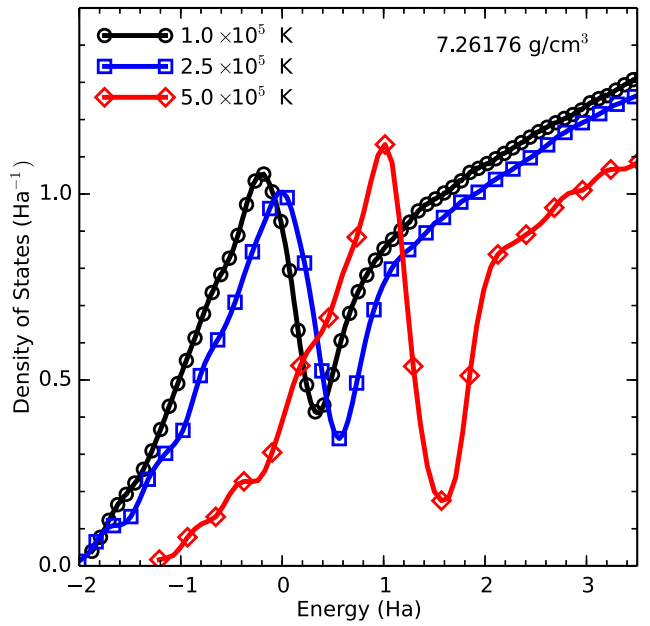

FIG. 11. Total electronic DOS of dense, fluid oxygen at a fixed density of 7.261 76 g cm^{-3} for three temperatures (1×10^5, 2.5×10^5, and 5×10^5 K). Each DOS curve has had the relevant Fermi energy for each temperature subtracted from it.

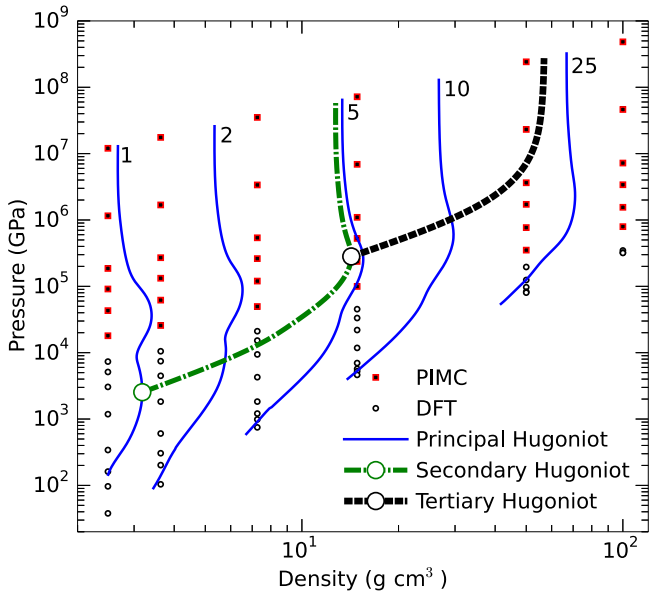

FIG. 12. Shock Hugoniot curves for different initial densities. The label on the curve specifies the ratio of the initial density to that of solid oxygen at 0 K, 0.6671 g cm^{-3}. Secondary and tertiary Hugoniot curves are also plotted.

as the initial state of the secondary Hugoniot curve. The compression maximum on this curve ($\rho = 14.25$ g cm^{-3}, $P = 282\,000$ GPa, $T = 4\,819\,000$ K) served as initial state for the tertiary Hugoniot curve.

Figure 13 shows the temperature dependence of the pre-compression density ratio for the five representative Hugoniot curves in Figure 12. In the high-temperature limit, all curves converge to a compression ratio of 4, which is the value of a nonrelativistic ideal gas. We also include of the Hugoniot curve computed with the relativistic, fully ionized Chabrier-Potekhin model, which shows the relativistic correction in the high-temperature limit. In general, the shock compression is determined by the excitation of internal degrees of freedom, which increases the compression, and interaction effects, which decrease the compression.[75] Consistent with our results for hydrogen, helium,[47] and neon,[50] we find that an increase

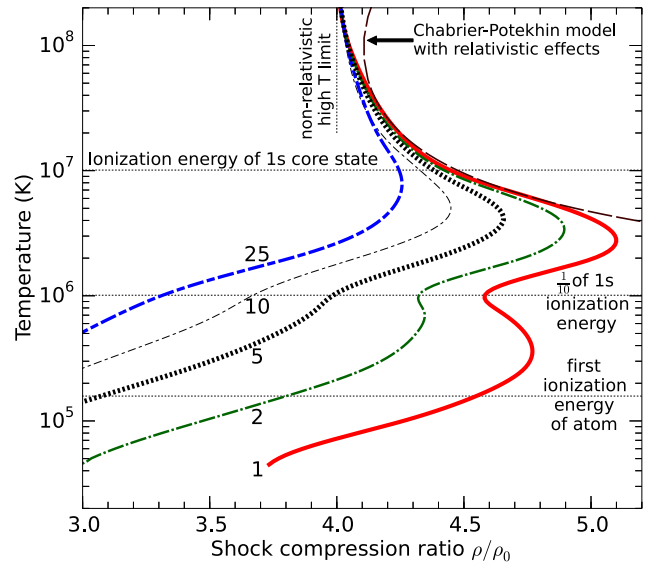

FIG. 13. Hugoniot curves for different pre-compression density ratios.

in the initial density leads to a slight reduction in the shock compression (Figure 13) because particles interact more strongly at higher density.

The shock-compression ratio also exhibits two maxima as a function of temperature, which can be attributed to the ionization of electrons in the first and second shells. On the principal Hugoniot curve, the first maximum of $\rho/\rho_0 = 4.77$ occurs at temperature of 3.59×10^5 K (30.94 eV), which is above the first ionization energy of the oxygen atom, 13.61 eV, but less than the second ionization energy, 35.12 eV. A second compression maximum of $\rho/\rho_0 = 5.10$ is found for a temperature of 2.87×10^6 K (247.32 eV), which can be attributed to the ionization of the 1s core states of the oxygen ions. The 1s ionization energy is 871.41 eV. This is consistent with the ionization process we observe in Figure 7, where charge density around the nuclei is reduced over the range of $2 - 8 \times 10^6$ K. Since DFT-MD simulations, which use pseudopotentials to replace core electrons, cannot access physics about core ionization, PIMC is a necessary tool to determine the maximum compression along the principle Hugoniot curve.

VII. CONCLUSIONS

In this work, we have combined PIMC with DFT-MD to construct a coherent EOS for oxygen over wide range of densities and temperatures that includes warm dense matter and plasmas in stars and stellar remnants. The two methods validate each other in temperature range of 2.5×10^5–1×10^6 K, where both yield consistent results. We compared our equation of state at high temperature with the analytic models of Chabrier-Potekhin and Debye-Hückel. The deviations that we identified underline the importance for new methods like PIMC to be developed for the study of warm dense matter. Nuclear and electronic pair-correlations reveal a temperature- and pressure-driven ionization process, where temperature-ionization of the 1s state is suppressed while other states are efficiently ionized as density increases up to 100 g cm^{-3}. Changes in the density of states confirm the temperature- and pressure-ionization behavior observed in the pair-correlation data. Finally, we find that the ionization imprints a signature on the shock Hugoniot curves and that PIMC simulations are necessary to determine the state of the highest shock compression. Our and Hugoniot and equation of state will help to build more accurate models for stars and stellar remnants.

ACKNOWLEDGMENTS

We are grateful to Alexander Potekhin for helpful discussions about the fully ionized EOS. We are also grateful to Cyril Georgy for sharing his data and knowledge of massive star evolution. We are also grateful to Jan Vorberger for discussions on continuum lowering. This research is supported by the U. S. Department of Energy, Grant No. DE-SC0010517. Computational support was provided by NERSC, NASA, and the Janus supercomputer, which is supported by the National Science Foundation (Grant No. CNS-0821794), the University of Colorado, and the National Center for Atmospheric Research.

[1]Y. A. Freiman and H. J. Jodl, Phys. Rep. **401**, 1 (2004).
[2]M. Santoro, E. Gregoryanz, H. k. Mao, and R. J. Hemley, Phys. Rev. Lett. **93**, 265701 (2004).
[3]L. F. Lundegaard, G. Weck, M. I. McMahon, S. Desgreniers, and P. Loubeyre, Nature **443**, 201 (2006).
[4]A. F. Goncharov, N. Subramanian, T. R. Ravindran, M. Somayazulu, V. B. Prakapenka, and R. J. Hemley, J. Chem. Phys. **135**, 084512 (2011).
[5]Y. Ma, A. R. Oganov, and C. W. Glass, Phys. Rev. B **76**, 064101 (2007).
[6]J. Sun, M. Martinez-Canales, D. D. Klug, C. J. Pickard, and R. J. Needs, Phys. Rev. Lett. **108**, 045503 (2012).
[7]S. Desgreniers, Y. K. vohra, and A. L. Ruoff, J. Phys. Chem. **94**, 1117 (1990).
[8]Y. Akahama, H. Kawamura, D. Häusermann, M. Hanfland, and O. Shimomura, Phys. Rev. Lett. **74**, 4690 (1995).
[9]S. Serra, G. Chiarotti, S. Scandolo, and E. Tosatti, Phys. Rev. Lett. **80**, 5160 (1998).
[10]B. Militzer and R. J. Hemley, Nature **443**, 150 (2006).
[11]K. Shimizu, K. Suhara, M. Ikumo, M. I. Eremets, and K. Amaya, Nature **393**, 767 (1998).
[12]J. B. Neaton and N. W. Ashcroft, Phys. Rev. Lett. **88**, 205503 (2002).
[13]S. Klotz, T. Strassle, A. L. Cornelius, J. Philippe, and T. Hansen, Phys. Rev. Lett. **104**, 115501 (2010).
[14]J. N. Bahcall and M. H. Pinsonneault, Phys. Rev. Lett. **92**, 121301 (2004).
[15]Private communication: Courtesy of Cyril Georgy, University of Keele (United Kingdom).
[16]G. Fontaine and H. M. V. Horn, Astrophys. J., Suppl. Ser. **31**, 467 (1976).
[17]G. Fontaine, H. C. J. Graboske, and H. M. V. Horn, Astrophys. J., Suppl. Ser. **35**, 293 (1977).
[18]B. Hansen, Phys. Rep. **399**, 1 (2004).
[19]A. Burrows, W. B. Hubbard, J. I. Lunine, and J. Liebert, Rev. Mod. Phys. **73**, 719 (2001).
[20]W. B. Hubbard, A. Burrows, and J. I. Lunine, Annu. Rev. Astron. Astrophys. **40**, 103 (2002).
[21]T. Guillot, Annu. Rev. Earth Planet. Sci. **33**, 493 (2005).
[22]H. F. Wilson and B. Militzer, Astrophys. J. **745**, 54 (2012).
[23]S. Zhang, H. F. Wilson, K. P. Driver, and B. Militzer, Phys. Rev. B **87**, 024112 (2013).
[24]C. Hansen and S. Kawaler, *Stellar Interiors: Physical Principles, Structure, and Evolution*, Astronomy and Astrophysics Library (Springer-Verlag, New York, 1994), Vol. 1.
[25]J. J. Fortney, Astrophys. J., Lett. **747**, L27 (2012).
[26]K. Lodders and J. B. Fegley, Icarus **155**, 393 (2002).
[27]M. Zoccali, A. Lecureur, B. Barbuy, V. Hill, A. Renzini, D. Minniti, Y. Momany, A. Gmez, and S. Ortolani, Astron. Astrophys. **457**, L1 (2006).
[28]M. H. Wong, J. I. Lunine, S. K. Atreya, T. Johnson, P. R. Mahaffy, T. C. Owen, and T. Ecnrenaz, Rev. Mineral. Geochem. **68**, 219 (2008).
[29]C. Needham, *Blast Waves*, Shock Wave and High Pressure Phenomena (Springer, Berlin Heidelberg, 2010).
[30]G. Wallerstein, I. Iben, P. Parker, A. Boesgaard, G. Hale, A. Champagne, C. Barnes, F. Käppeler, V. Smith, R. Hoffman, F. Timmes, C. Sneden, R. Boyd, B. Meyer, and D. Lambert, Rev. Mod. Phys. **69**, 995 (1997).
[31]E. M. Burbidge, G. R. Burbidge, W. a. Fowler, and F. Hoyle, Rev. Mod. Phys. **29**, 547 (1957).
[32]M. Schmidt, Astrophys. J. **129**, 243 (1959).
[33]G. Fontaine, P. Brassard, and P. Bergeron, Publ. Astron. Soc. Pac. **113**, 409 (2001).
[34]G. Chabrier, P. Brassard, G. Fontaine, and D. Saumon, Astrophys. J. **543**, 216 (2000).
[35]K. Lodders, Astrophys. J. **591**, 1220 (2003).
[36]N. Itoh, K. Kojo, and M. Nakagawa, Astrophys. J., Suppl. Ser. **74**, 291 (1990).
[37]M. Bastea, A. C. Mitchell, and W. J. Nellis, Phys. Rev. Lett. **86**, 3108 (2001).
[38]B. Militzer, F. Gygi, and G. Galli, Phys. Rev. Lett. **91**, 265503 (2003).
[39]W. J. Nellis and A. C. Mitchell, J. Chem. Phys. **73**, 6137 (1980).
[40]D. C. Hamilton, W. J. Nellis, A. Mitchell, F. H. Ree, and M. van Thiel, J. Chem. Phys. **88**, 5042 (1988).
[41]E. D. Chisolm, S. D. Crockett, and M. S. Shaw, AIP Conf. Proc. **1195**, 556 (2009).
[42]M. Ross and F. H. Ree, J. Chem. Phys. **73**, 6146 (1980).
[43]G. I. Kerley and A. C. Awitendick, in *Shock Waves in Condensed Matter*, edited by Y. M. Gupta (Plenum, New York, 1986).
[44]Q. F. Chen, L. C. Cai, Y. Zhang, and Y. J. Gu, J. Chem. Phys. **128**, 104512 (2008).
[45]C. Wang and P. Zhang, J. Chem. Phys. **132**, 154307 (2010).
[46]G. Massacrier, A. Y. Potekhin, and G. Chabrier, Phys. Rev. E: Stat., Nonlinear, Soft Matter Phys. **84**, 1 (2011).

[47]B. Militzer, Phys. Rev. B **79**, 155105 (2009).
[48]K. P. Driver and B. Militzer, Phys. Rev. Lett. **108**, 115502 (2012).
[49]L. X. Benedict, K. P. Driver, S. Hamel, B. Militzer, T. Qi, A. A. Correa, and E. Schwegler, Phys. Rev. B **89**, 224109 (2014).
[50]K. P. Driver and B. Militzer, Phys. Rev. B **91**, 045103 (2015).
[51]D. M. Ceperley, Rev. Mod. Phys. **67**, 279 (1995).
[52]M. Koenig *et al.*, Plasma Phys. Controlled Fusion **47** (2005).
[53]E. L. Pollock, Comput. Phys. Commun. **52**, 49 (1988).
[54]D. M. Ceperley, J. Stat. Phys. **63**, 1237 (1991).
[55]B. Militzer and D. M. Ceperley, Phys. Rev. E **63**, 066404 (2001).
[56]See supplementary material at http://dx.doi.org/10.1063/1.4934348 for time-step and finite-size convergence tables.
[57]D. Marx, J. Hutter, in *Modern Methods and Algorithms of Quantum Chemistry Proceedings*, 2nd ed., edited by J. Grotendorst (John von Neumann Institute for Computing, Forschungszentrum Julich, Germany, 2000), NIC series, Vol. 3, pp. 329–477.
[58]E. W. Brown, B. K. Clark, J. L. DuBois, and D. M. Ceperley, Phys. Rev. Lett. **110**, 146405 (2013).
[59]D. N. Mermin, Phys. Rev. **137**, A1441 (1965).
[60]F. Lambert, J. Clérouin, and S. Mazevet, Europhys. Lett. **75**, 681 (2006).
[61]G. Kresse and J. Furthmüller, Phys. Rev. B **54**, 11169 (1996).
[62]P. E. Blöchl, Phys. Rev. B **50**, 17953 (1994).
[63]J. P. Perdew, K. Burke, and M. Ernzerhof, Phys. Rev. Lett. **77**, 3865 (1996).
[64]X. Gonze, B. Amadon, P. M. Anglade, J. M. Beuken, F. Bottin, P. Boulanger, F. Bruneval, D. Caliste, R. Caracas, M. Côté, T. Deutsch, L. Genovese, P. Ghosez, M. Giantomassi, S. Goedecker, D. R. Hamann, P. Hermet, F. Jollet, G. Jomard, S. Leroux, M. Mancini, S. Mazevet, M. J. T. Oliveira, G. Onida, Y. Pouillon, T. Rangel, G. M. Rignanese, D. Sangalli, R. Shaltaf, M. Torrent, M. J. Verstraete, G. Zerah, and J. W. Zwanziger, Comput. Phys. Commun. **180**, 2582 (2009).
[65]N. A. W. Holzwarth, A. R. Tackett, and G. E. Matthews, Comput. Phys. Commun. **135**, 329 (2001).
[66]See http://elk.sourceforge.net/ for the source code and manual.
[67]G. Chabrier and A. Y. Potekhin, Phys. Rev. E **58**, 4941 (1998).
[68]P. Debye and E. Huckel, Phys. Z. **24**, 185 (1923).
[69]See http://opium.sourceforge.net for the source code and manual.
[70]B. Militzer, J. Phys. A: Math. Theor. **42**, 214001 (2009).
[71]*Photoemission in Solids I: General Principles*, edited by M. Cardona and L. Ley (Springer-Verlag, Berlin, 1978).
[72]S. Root, R. J. Magyar, J. H. Carpenter, D. L. Hanson, and T. R. Mattsson, Phys. Rev. Lett. **105**, 085501 (2010).
[73]Y. B. Zeldovich and Y. P. Raizer, *Elements of Gasdynamics and the Classical Theory of Shock Waves* (Academic Press, New York, 1968).
[74]B. Militzer and W. B. Hubbard, AIP Conf. Proc. **955**, 1395 (2007).
[75]B. Militzer, Phys. Rev. Lett. **97**, 175501 (2006).